Article

Synthesis of a semimetallic Weyl ferromagnet with point Fermi surface

https://doi.org/10.1038/s41586-024-08330-y

Received: 24 February 2024

Accepted: 31 October 2024

Published online: 22 January 2025

Check for updates

Ilya Belopolski[1,12]✉, Ryota Watanabe[2,3,12], Yuki Sato[1], Ryutaro Yoshimi[1], Minoru Kawamura[1], Soma Nagahama[2,3], Yilin Zhao[4], Sen Shao[4], Yuanjun Jin[4], Yoshihiro Kato[2,3], Yoshihiro Okamura[2,3], Xiao-Xiao Zhang[1,5,6], Yukako Fujishiro[1,7], Youtarou Takahashi[1,2,3], Max Hirschberger[1,2,3], Atsushi Tsukazaki[8], Kei S. Takahashi[1], Ching-Kai Chiu[9], Guoqing Chang[4], Masashi Kawasaki[1,2,3], Naoto Nagaosa[1,10] & Yoshinori Tokura[1,2,3,11]✉

Quantum materials governed by emergent topological fermions have become a cornerstone of physics. Dirac fermions in graphene form the basis for moiré quantum matter and Dirac fermions in magnetic topological insulators enabled the discovery of the quantum anomalous Hall (QAH) effect[1–3]. By contrast, there are few materials whose electromagnetic response is dominated by emergent Weyl fermions[4–6]. Nearly all known Weyl materials are overwhelmingly metallic and are largely governed by irrelevant, conventional electrons. Here we theoretically predict and experimentally observe a semimetallic Weyl ferromagnet in van der Waals $(Cr,Bi)_2Te_3$. In transport, we find a record bulk anomalous Hall angle of greater than 0.5 along with non-metallic conductivity, a regime that is strongly distinct from conventional ferromagnets. Together with symmetry analysis, our data suggest a semimetallic Fermi surface composed of two Weyl points, with a giant separation of more than 75% of the linear dimension of the bulk Brillouin zone, and no other electronic states. Using state-of-the-art crystal-synthesis techniques, we widely tune the electronic structure, allowing us to annihilate the Weyl state and visualize a unique topological phase diagram exhibiting broad Chern insulating, Weyl semimetallic and magnetic semiconducting regions. Our observation of a semimetallic Weyl ferromagnet offers an avenue towards new correlated states and nonlinear phenomena, as well as zero-magnetic-field Weyl spintronic and optical devices.

Semiconductors and semimetals are materials in which electrons show behaviour between that in insulators and metals. Although semiconductors form the basis for modern electronics, and semimetals have been at the frontier of quantum physics for two decades, surprisingly, the interplay between these two fundamental phases of matter remains little explored[1–3,7]. Here we report a magnetic Weyl semimetal achieved by chemical engineering of a semiconductor. Our measurements suggest that the quantum electronic structure of our material, bismuth telluride doped with chromium, or $(Cr,Bi)_2Te_3$, has a Fermi surface composed entirely of Weyl points. This places our material in a unique limit of both vanishing carrier concentration and vanishing energy gap. Only a few quantum materials are known in this extreme semimetallic regime[8]. Typical semimetals have a gapless electronic structure with a finite concentration of charge carriers. Established Weyl materials are semimetals in this weaker sense, hosting substantial irrelevant charge carriers that coexist with the Weyl fermions and obscure their unique properties. As a result, investigations so far rely on momentum-resolved spectroscopic probes or sophisticated analysis of quantum oscillations[4–6,9]. Trivial, metallic electrons are intrinsic to the TaAs family of inversion-breaking Weyl materials; the RhSi family of topological chiral crystals; ferromagnetic Weyl kagome $Co_3Sn_2S_2$; and linked Weyl ring Co_2MnGa (refs. 4–6,10). By contrast, a material with only Weyl points at the Fermi level will exhibit electromagnetic response dominated by Weyl physics. Such a semimetallic Weyl material is of urgent interest and expected to support new device functionality, including topological transistors[5,11], giant photovoltaic effects[12], Weyl spin-charge switches[13], nonlinear terahertz components[14,15], Majorana–Fermi arcs[16], energy-harvesting thermoelectrics[17,18] and topological catalysts[19]. A Fermi surface of only Weyl points is further expected to fail to screen Coulomb repulsion, producing a logarithmically divergent correction to Fermi velocities[20–23] and emergent Lorentz invariance driven by interactions[24].

To realize a semimetallic Weyl phase of matter, it is natural to start from a semiconductor, without irrelevant metallic bands anywhere in the Brillouin zone. Chemical substitution can then introduce ferromagnetism, breaking time-reversal symmetry and producing a Zeeman

[1]RIKEN Center for Emergent Matter Science (CEMS), Wakō, Japan. [2]Department of Applied Physics, University of Tokyo, Tokyo, Japan. [3]Quantum-Phase Electronics Center (QPEC), University of Tokyo, Tokyo, Japan. [4]Division of Physics and Applied Physics, School of Physical and Mathematical Sciences, Nanyang Technological University, Singapore, Singapore. [5]Wuhan National High Magnetic Field Center, Huazhong University of Science and Technology, Wuhan, China. [6]School of Physics, Huazhong University of Science and Technology, Wuhan, China. [7]RIKEN Cluster for Pioneering Research (CPR), Wakō, Japan. [8]Institute for Materials Research, Tohoku University, Sendai, Japan. [9]RIKEN Interdisciplinary Theoretical and Mathematical Sciences Program (iTHEMS), Wakō, Japan. [10]Fundamental Quantum Science Program, TRIP Headquarters, RIKEN, Wakō, Japan. [11]Tokyo College, University of Tokyo, Tokyo, Japan. [12]These authors contributed equally: Ilya Belopolski, Ryota Watanabe. ✉e-mail: ilya.belopolski@riken.jp; tokura@riken.jp

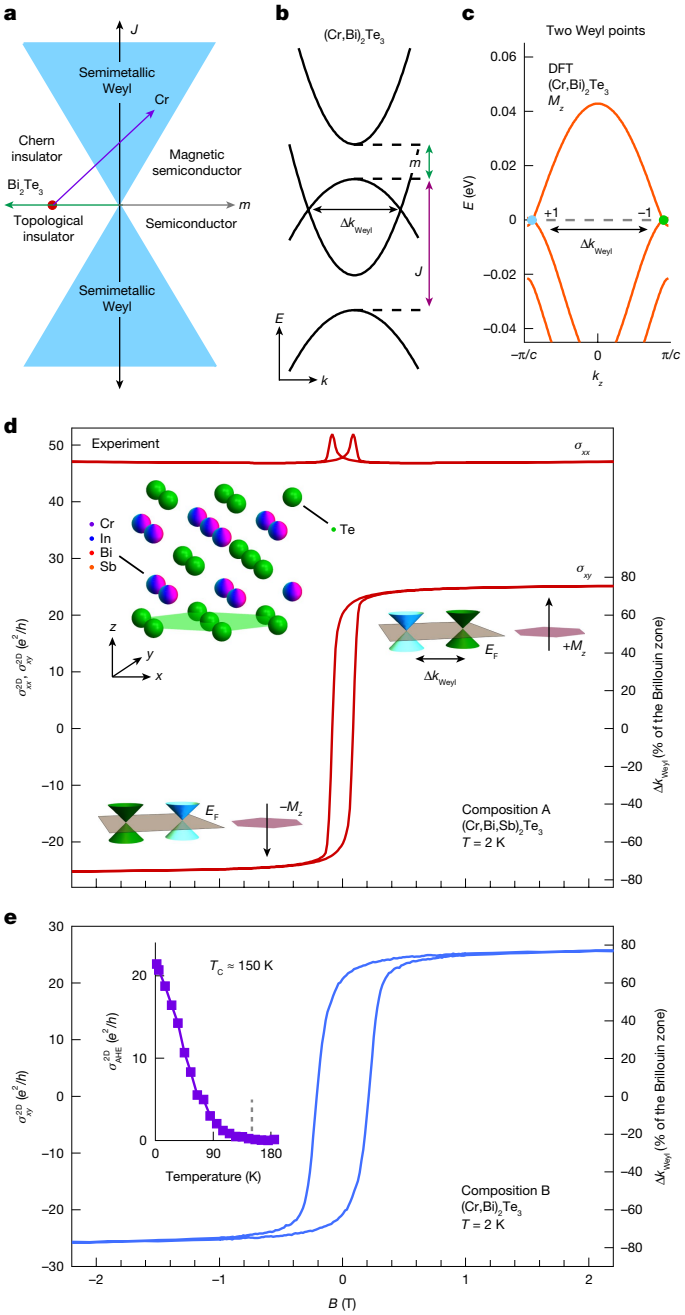

Fig. 1 | Weyl transport semimetal in $(Cr,Bi)_2Te_3$. **a**, Phase diagram for a semiconductor with mass gap m and ferromagnetic exchange splitting J. This diagram can be viewed as the magnetic analogue to the Murakami phase diagram for a Weyl semimetal[30]. **b**, Bi_2Te_3 is a topological insulator, with $m < 0$, $J = 0$. Cr doping introduces ferromagnetism and reduces the SOC, driving a band inversion and forming a semimetallic phase with two Weyl points. **c**, The electronic structure of $(Cr,Bi)_2Te_3$ under ferromagnetic order, from ab initio calculations. The Fermi surface shows two Weyl points, with separation $\Delta k_{Weyl} \approx 90\%$. **d**, Longitudinal, σ_{xx}^{2D}, and Hall, σ_{xy}^{2D}, sheet conductivity of $(Cr,Bi,Sb)_2Te_3$, composition A, with sample thickness $h = 100$ nm. From symmetry analysis (see main text), the Fermi surface is composed of two Weyl points, so we can directly convert the AHE into a Weyl point separation, $\Delta k_{Weyl} \approx 75\%$ of the bulk Brillouin zone along k_z. Inset, the chromium (Cr), indium (In), bismuth (Bi) and antimony (Sb) dopants randomly occupy the cation site of the Bi_2Te_3 crystal structure. **e**, Hall sheet conductivity σ_{xy}^{2D} for $(Cr,Bi)_2Te_3$, composition B, showing $\Delta k_{Weyl} \approx 77\%$. Inset, temperature dependence of the AHE, indicating a Curie temperature $T_C \approx 150$ K.

Table 1 | Weyl compositions

Composition	Cr	In	Sb	Bi	Δk_{Weyl}
A	0.24	0	0.20	0.56	75%
B	0.30	0	0	0.70	77%
C	0.13	0.02	0.57	0.28	15%
D	0.05	0	0.64	0.31	Chern
E	0.27	0.06	0.45	0.22	Trivial
calc.	0.33	0	0	0.67	90%
calc.	0.33	0	0.67	0	11%

Representative samples examined in the present work, all based on $(Cr,Bi)_2Te_3$. The values are written as $(Cr_xIn_yBi_zSb_{1-x-y-z})_2Te_3$. A further 34 measured devices are marked in Fig. 3b. Weyl point separation is given as % along k_z of the Brillouin zone of the conventional unit cell.

splitting that can drive the formation of emergent Weyl fermions[7]. Using a semiconductor with large spin–orbit coupling (SOC) may also give wider access to the topological phase space (Fig. 1a). Although such a scheme was at the core of early proposals for Weyl semimetals[25–32], these proposals have not yet been experimentally realized. Bi_2Te_3 is a topological semiconductor that has already been ferromagnetically doped to produce a QAH state[3]. To produce Weyl fermions in Bi_2Te_3, it is necessary to introduce a ferromagnetic exchange splitting J, sending the material from the topological insulating state towards a semimetallic Weyl state. It may also be beneficial to increase the mass gap m by reducing the SOC. Notably, both can be achieved by chemically substituting Cr into pristine Bi_2Te_3 (Fig. 1b).

Weyl semimetal in $(Cr,Bi)_2Te_3$

We synthesized films of Bi_2Te_3 doped with Cr, with a further low level of Sb co-doping to achieve charge neutrality (composition A, Table 1). Note that this composition includes much higher Cr content than is typically used to produce a QAH state and can only be achieved by low-temperature non-equilibrium molecular beam epitaxy[3,33]. In transport, we first examine the two-dimensional Hall sheet conductivity $\sigma_{xy}^{2D}(B)$ of such a $(Cr,Bi,Sb)_2Te_3$ film, of thickness $h = 100$ nm (Fig. 1d). We obtain the anomalous Hall effect (AHE) σ_{AHE}^{2D} at $T = 2$ K by extrapolating the high-magnetic-field $\sigma_{xy}^{2D}(B)$ back to zero field. We find $\sigma_{AHE}^{2D} \approx 24\ e^2/h$, written in units of the conductance quantum $e^2/h \approx 3.9 \times 10^{-5}\ \Omega^{-1}$ (Extended Data Fig. 9). This result is unexpected because topological insulators with ferromagnetism typically exhibit a QAH generated by magnetically gapped Dirac cone surface states. In this well-known scenario, σ_{AHE}^{2D} can never exceed $1\ e^2/h$. Our observation of $\sigma_{AHE}^{2D} \gg 1\ e^2/h$ suggests that the observed Hall effect is instead driven by bulk Berry curvature. Because Cr doped into Bi_2Te_3 introduces ferromagnetism and reduces SOC, it naturally drives a transition from a topological insulator to a Weyl semimetal[28,30]. To theoretically understand this phase transition, we can consider a minimal $k{\cdot}p$ model for Bi_2Te_3 describing the electronic structure in the vicinity of the bulk Γ point[34,35]. In the presence of ferromagnetism, to linear order in k, the low-energy electronic structure is governed by

$$h(\mathbf{k})_{(Cr,Bi)_2Te_3} = v_F(\mathbf{k}\cdot\sigma)\tau_x + m\tau_z + J\sigma_z \quad (1)$$

in which $\mathbf{k}$ is the crystal momentum, σ acts in spin space, τ acts in orbital space, m sets the mass gap and J sets the ferromagnetic exchange splitting. Suppose that the mass gap is positive far from Γ, at all other time-reversal invariant momenta. Then, pristine Bi_2Te_3 has $m < 0$, $J = 0$, giving a band inversion at Γ, which produces a three-dimensional $\mathbb{Z}_2$ topological insulator. The case $m > 0$ would correspond to a trivial insulator. Ferromagnetic $(Cr,Bi)_2Te_3$ is a Weyl semimetal whenever the exchange splitting J overwhelms the mass gap m, with exactly two Weyl points along the k_z axis at $v_F^2k_z^2 = J^2 - m^2$.

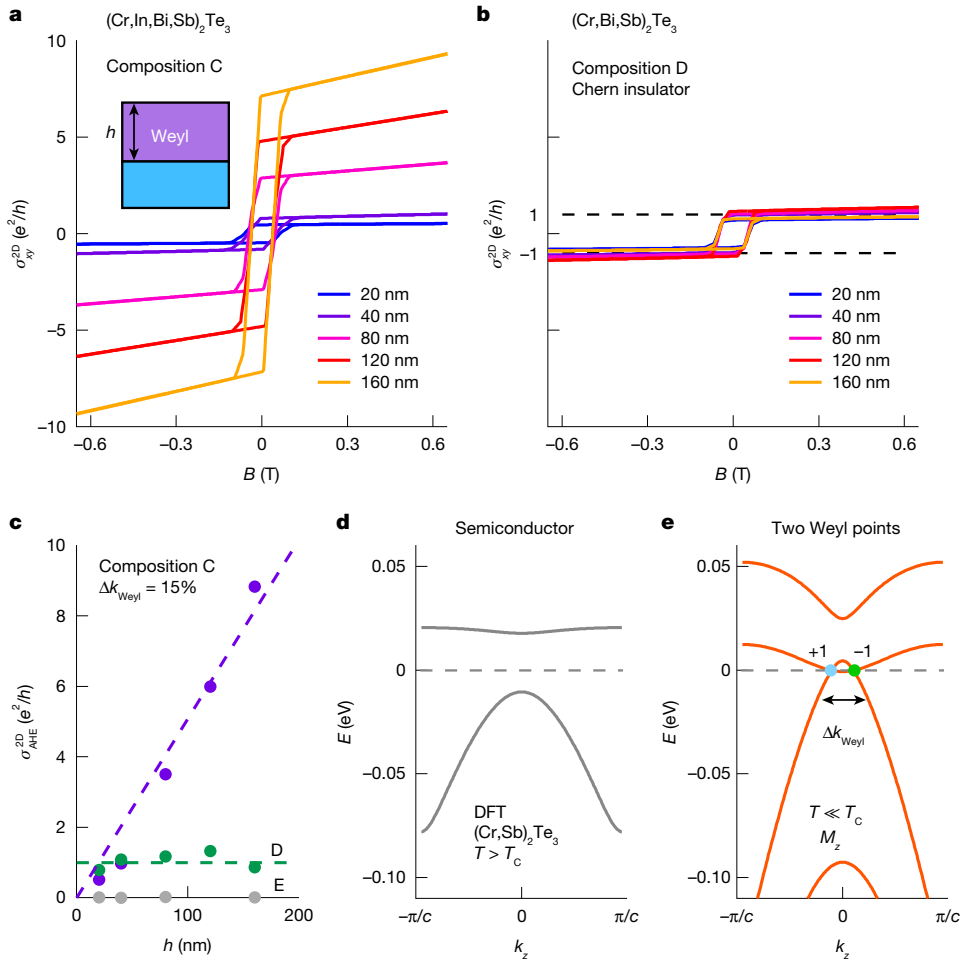

Fig. 2 | Tunability of a semimetallic Weyl state. Hall sheet conductivity σ_{xy}^{2D} as a function of film thickness h for $(Cr,In,Bi,Sb)_2Te_3$ in the Weyl phase (**a**, composition C) and $(Cr,Bi,Sb)_2Te_3$ in the Chern insulator phase (**b**, composition D) at $T = 2$ K. **c**, Scaling of the AHE with h, showing sharply contrasting bulk scaling (composition C) and surface scaling (composition D). Composition E is a topologically trivial magnetic semiconductor $(In,Cr,Bi,Sb)_2Te_3$, showing zero AHE (see Extended Data Fig. 2). Ab initio calculation of $(Cr,Sb)_2Te_3$, without magnetic order, showing a semiconducting electronic structure (**d**) and under ferromagnetism, showing two Weyl points with magnetic order, $\Delta k_{Weyl} \approx 11\%$, roughly in agreement with $\Delta k_{Weyl} \approx 15\%$ measured for composition C (**e**).

Crucially, Bi_2Te_3 has no irrelevant electronic states near the Fermi level elsewhere in the bulk Brillouin zone. As a result, if the system is tuned to charge neutrality, the Fermi surface consists of only two Weyl points. Furthermore, recall that the AHE in a Weyl semimetal is proportional to the separation of the Weyl points in momentum space $\sigma_{xy}^{3D} = (\Delta k/2\pi)(e^2/h)$ (ref. 36). In our case, this implies that we can extract the Weyl point separation directly from the measured Hall conductivity, when the system is tuned to charge neutrality. For composition A′ we find a separation of about 75% of the bulk Brillouin zone in the k_z direction (Fig. 1d, right axis), larger than any Weyl material studied so far.

Large Weyl point separation

To more deeply understand this large Weyl point separation, we performed ab initio calculations of $(Cr,Bi)_2Te_3$. We observe two Weyl points at the Fermi level, with a large separation of about 90% of the Brillouin zone, broadly consistent with our experiment (Fig. 1c). Examining the measured longitudinal conductivity, we find a relatively small value, $\sigma_{xx}^{2D} \approx 47\ e^2/h$, giving a Hall angle, $\sigma_{AHE}/\sigma_{xx} \approx 0.51$, again larger than any Weyl material studied so far. We can naturally understand the giant bulk Hall angle given the simplicity of our system, which shows the minimum number of Weyl points, with no irrelevant electronic states at the Fermi level and chemical potential tuned to charge neutrality. This transport data, theoretical analysis and ab initio calculation together suggest the observation of a semimetallic Weyl ferromagnet in $(Cr,Sb,Bi)_2Te_3$. Despite numerous theoretical proposals and experimental attempts over the course of more than a decade, a magnetic Weyl semimetal has never before been produced from a semiconductor[25,26,28,29]. We can simplify the film composition by using Cr alone to introduce ferromagnetism, suppress SOC and bring the material towards charge neutrality. In $(Cr,Bi)_2Te_3$, composition B, we again observe $\sigma_{xy} \gg 1\ e^2/h$, with Weyl point separation of approximately 77% (Fig. 1e). The large Cr level in our semimetallic Weyl films further drives a large Curie temperature $T_C \approx 150$ K (Fig. 1e, inset) and enhanced coercive field, indicating a robust ferromagnetic Weyl phase.

To more carefully demonstrate a semimetallic Weyl ferromagnet, we examine the transport properties of our films as a function of thickness. Here we also co-dope with a low level of indium, In, which predominantly serves to reduce the SOC. This allows us to use a lower Cr level and consider two compositions that are chemically similar, but with $(In,Cr,Bi,Sb)_2Te_3$, composition C, targeting a semimetallic Weyl state and a nearby $(Cr,Bi,Sb)_2Te_3$, composition D, targeting a Chern insulator (Table 1). For both compositions, we maintain approximate charge neutrality at a ratio Bi:Sb ≈ 1:2. We observe that the series of films in composition C exhibit a Hall sheet conductance that scales linearly with the film thickness, indicating an AHE driven by bulk

Berry curvature (Fig. 2a,c). By contrast, the series in composition D exhibits an AHE quantized to $\pm 1\, e^2/h$ regardless of the film thickness, indicating that the Hall response is driven by the top and bottom surfaces of the film (Fig. 2b). We can again extract the Weyl point separation for our $(In,Cr,Bi,Sb)_2Te_3$ Weyl films, for which we observe a modest $\Delta k_{Weyl} \approx 15\%$ of the Brillouin zone, consistent with the lower Cr level and consequently weaker ferromagnetism. As an extra check, we examine a more heavily In-doped composition E, which shows no appreciable AHE, suggesting the absence of Berry curvature and indicating a topologically trivial magnetic semiconductor (Extended Data Fig. 2). We also perform ab initio calculations for Cr-substituted Sb_2Te_3, which more closely captures the high Sb level of composition C. We obtain $\Delta k_{Weyl} \approx 11\%$ (Fig. 1d,e and Extended Data Fig. 7), roughly in agreement with transport. We further explore the Faraday rotation of composition C in terahertz spectroscopy, which is directly sensitive to the bulk topological nature of the system[37] (Extended Data Fig. 5). We observe an optical response consistent with dc transport, providing independent experimental evidence for a semimetallic Weyl ferromagnet.

Topological phase diagram

We can more deeply explore the Weyl state through the chiral anomaly, which gives rise to a negative longitudinal magnetoresistance under parallel electric and magnetic fields[27,38]. We measure the longitudinal resistivity under in-plane magnetic field B, as a function of the angle θ between the applied current I and B, for films with varying Cr and In levels (Fig. 3a). We find that the Chern insulator composition D exhibits a maximum in the resistivity under $I \| B$, which is the typical magnetoresistance anisotropy observed in conventional magnets, as well as topological insulators[39]. We observe a similar behaviour in composition E, targeting a topologically trivial magnetic semiconducting state. By contrast, the Weyl composition C exhibits a suppression of the resistivity under parallel I and B, suggesting a contribution from the chiral anomaly. Note that the typical mobilities we achieve here are comparable with those of Na_3Bi, in which current jetting gives only a small correction to the negative magnetoresistance[40]. To further explore the chiral anomaly, we make use of (In,Cr) doping to precisely vary the ferromagnetism and SOC throughout the topological phase diagram, across a library of 37 films (including A, C, D and E; Fig. 3b). At low (In,Cr), corresponding to a Chern insulator, and at high (In,Cr), corresponding to a trivial magnetic semiconductor, we observe a conventional, positive magnetoresistance anisotropy (colour map in Fig. 3b obtained from $\Delta\rho_{xx}(\theta = 0°)$ measured at each black dot). At intermediate Cr levels, we consistently observe a negative magnetoresistance anisotropy, suggesting a chiral anomaly driven by the Weyl phase.

To gain further insight into our composition map, we consider the topological phase diagram of our system. Our low-energy effective theory, equation (1), reveals Weyl semimetal phases separating Chern and trivial insulator phases as a function of J and m. The phase boundaries are at $J = \pm m$ (black lines, Fig. 3c). To relate our colour map of the chiral anomaly to our theoretical phase diagram, again recall that Cr doping both introduces ferromagnetism and reduces SOC, whereas In doping only reduces SOC. We can therefore convert the (In, Cr) axes to (magnetism, SOC) axes by means of a linear coordinate transformation, in a way that associates the positive and negative magnetoresistance regions with the topological phases. Under a reasonable linear coordinate transformation, we find that the negative magnetoresistance region coincides well with the Weyl phase, whereas the positive regions coincide well with the Chern insulator and magnetic semiconductor phases (Fig. 3c). To better understand this correspondence, we numerically calculate the Chern number for a lattice model of our Weyl semimetal (see Methods and Supplementary Figs. 1 and 2). As we vary J and m, we numerically observe a plateau at

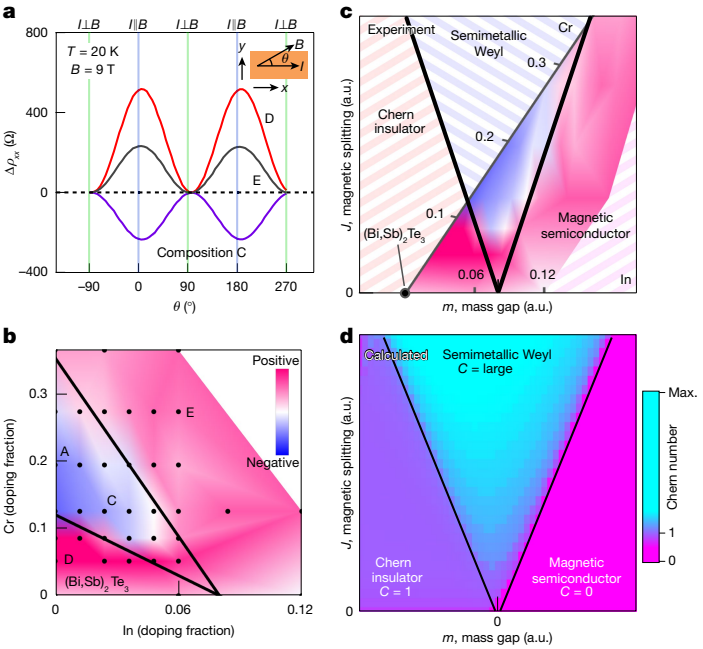

Fig. 3 | Experimental visualization of the topological phase diagram. **a**, Angle dependence of the magnetoresistance, $\Delta\rho_{xx}(\theta) = \rho_{xx}(\theta) - \rho_{xx}(\theta = 90°)$, showing negative angular magnetoresistance for the semimetallic Weyl phase (composition C) and positive angular magnetoresistance for the topological (composition D) and trivial (composition E) insulating phases. Inset, measurement geometry. **b**, Systematic composition dependence of the angular magnetoresistance across 37 films (black dots), $h = 20$ nm, with varying In and Cr content. The colour map is obtained from the measured $\Delta\rho_{xx}(\theta = 0°)$ at each black dot, revealing large regions with negative (blue) and positive (red) angular magnetoresistance. **c**, The original Murakami phase diagram considers a Weyl semimetal driven by inversion breaking[30]. The magnetic analogue to the Murakami diagram has ferromagnetic exchange splitting J, breaking time-reversal symmetry. Coordinate transformation of the colour map in **b** from (In,Cr) composition axes to (m,J) axes. Note that In predominantly suppresses the SOC, increasing m from negative to positive, and Cr introduces ferromagnetism and suppresses SOC, increasing both J and m. **d**, Numerical calculation of the Chern number for a finite-size lattice model, exhibiting Chern insulator $C = 1$, semimetallic Weyl $C > 1$ and magnetic semiconductor $C = 0$ phases (see Methods). a.u., arbitrary units.

$C = 0$ for the trivial magnetic semiconductor region; a $C = 1$ plateau for the Chern insulator; and bulk scaling of C for the Weyl semimetal (Fig. 3d). These regions are also consistent with the experimental bulk scaling of the AHE for Weyl composition C, surface scaling of the QAH in composition D and absence of AHE in semiconductor composition E (Fig. 2c). Taken together, our results show that we access broad regions of the semimetallic Weyl, Chern insulator and magnetic semiconductor phase space. Our phase diagram deepens our fundamental understanding of these topological phases but has so far been theoretically overlooked. It can be viewed as analogous to the inversion-breaking phase diagram proposed by Murakami but instead with broken time-reversal symmetry[30]. Our systematic measurements further allow us to experimentally visualize this canonical magnetic topological phase diagram for the first time.

Large Hall angle, σ_{AHE}/σ_{xx}

A decade of exploration of Weyl physics in quantum matter has led to the discovery of numerous materials with unusual properties[4–6,27]. However, far from being semimetallic, nearly all of these materials are dominated by conventional metallic response (Fig. 4a). Our systematic transport measurements and chemical composition dependence,

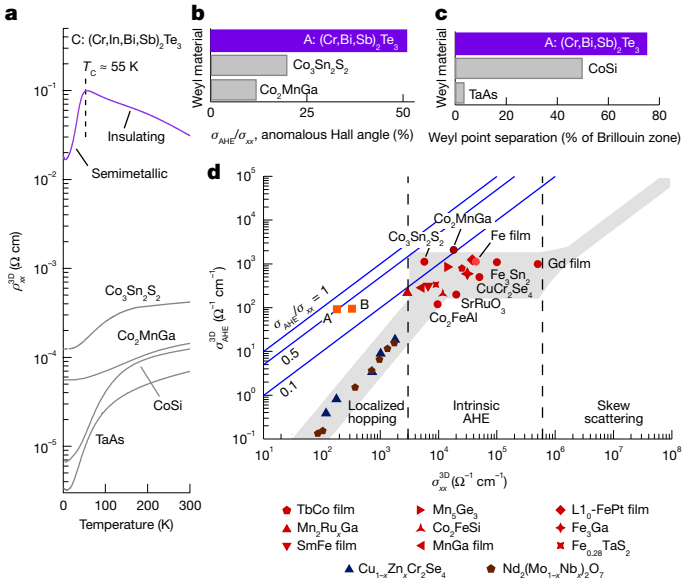

Fig. 4 | Large Weyl point separation and large anomalous Hall angle. a, The conventionally best-established Weyl materials exhibit metallic resistivity $\rho_{xx}(T)$ owing to irrelevant, conventional electrons in the electronic structure (grey). For our semimetallic Weyl system, $\rho_{xx}(T)$ is substantially enhanced, characteristic of a transport semimetal (purple, $h = 100$ nm). Our $(Cr,Bi)_2Te_3$ platform further exhibits anomalous Hall angle up to $\sigma_{AHE}/\sigma_{xx} = 0.51$ (**b**) and Weyl point separation up to 75% of the Brillouin zone, substantially larger than all existing Weyl materials (**c**). **d**, Map of σ_{AHE} versus σ_{xx} for several ferromagnets[42,43], illustrating the typical regimes of the localized hopping, intrinsic and skew scattering mechanisms[41]. In the present case, $(Cr,Bi)_2Te_3$ shows intrinsic AHE but lies outside the typical intrinsic regime, owing to the Weyl point Fermi surface, with enhanced anomalous Hall angle. Data points for A and B obtained from Fig. 1d,e, $T = 2$ K.

combined with ab initio calculations and analytical theory, show that $(Cr,Bi)_2Te_3$ offers a semimetallic Weyl quantum material. In strong contrast to existing Weyl materials, this platform is based on a semiconductor and exhibits a Weyl point Fermi surface. Examining $\rho_{xx}(T)$, we directly observe an insulating behaviour above the Curie temperature, $T > T_C$, suggestive of a semiconductor, followed by a decrease in the resistivity at $T < T_C$ as the ferromagnetism drives a Weyl state (Fig. 4a and Extended Data Figs. 6,8). We further observe a giant Hall angle $\tan\theta_H = \sigma_{AHE}/\sigma_{xx} = 0.51$ at our optimal composition, more than double existing Weyl materials, again suggesting a semimetallic Fermi surface (Fig. 4b). We also find an exceptionally large separation of Weyl points, suggesting that $(Cr,Bi)_2Te_3$ offers a robust and highly tunable semimetallic Weyl platform (Fig. 4c). Last, we consider $(Cr,Bi)_2Te_3$ in the context of the unified scaling relations governing σ_{AHE} and σ_{xx} (ref. 41). Materials typically fall into one of three regimes: a high-conductivity skew scattering regime; a low-conductivity localized hopping regime; and an intermediate regime governed by Berry curvature, with $\sigma_{xx} \approx 10^4$ to $10^6\ \Omega^{-1}\,cm^{-1}$ (Fig. 4d). Although σ_{AHE} in $(Cr,Bi)_2Te_3$ is produced by Berry curvature, the low σ_{xx} drives the system outside the conventional regime of the intrinsic AHE, with $\sigma_{xx} \approx 10^2\ \Omega^{-1}\,cm^{-1}$. This unique behaviour is again a direct consequence of electromagnetic response dominated by Weyl fermions, rather than conventional accumulation of Berry curvature in the electronic structure. The synthesis of a semimetallic Weyl quantum material, with a Fermi surface consisting only of Weyl points, offers unprecedented opportunities to incorporate emergent Weyl fermions into device architectures. Such a semimetallic system also offers opportunities to investigate breakdown of the Fermi liquid picture and renormalization of Fermi velocities[20–23], arising from the interplay of emergent Weyl fermions and electron–electron interactions.

Online content

Any methods, additional references, Nature Portfolio reporting summaries, source data, extended data, supplementary information, acknowledgements, peer review information; details of author contributions and competing interests; and statements of data and code availability are available at https://doi.org/10.1038/s41586-024-08330-y.

1. Anirban, A. 15 years of topological insulators. *Nat. Rev. Phys.* **5**, 267 (2023).
2. Tokura, Y. Quantum materials at the crossroads of strong correlation and topology. *Nat. Mater.* **1**, 971–973 (2022).
3. Tokura, Y., Yasuda, K. & Tsukazaki, A. Magnetic topological insulators. *Nat. Rev. Phys.* **1**, 126–143 (2019).
4. Armitage, N. P., Mele, E. J. & Vishwanath, A. Weyl and Dirac semimetals in three-dimensional solids. *Rev. Mod. Phys.* **90**, 015001 (2018).
5. Hasan, M. Z. et al. Weyl, Dirac and high-fold chiral fermions in topological quantum matter. *Nat. Rev. Mater.* **6**, 784–803 (2021).
6. Bernevig, B. A., Felser, C. & Beidenkopf, H. Progress and prospects in magnetic topological materials. *Nature* **603**, 41–51 (2022).
7. Ohno, H. Making nonmagnetic semiconductors ferromagnetic. *Science* **281**, 951–956 (1998).
8. Santos-Cottin, D. et al. $EuCd_2As_2$: a magnetic semiconductor. *Phys. Rev. Lett.* **131**, 186704 (2023).
9. Guo, C. et al. Temperature dependence of quantum oscillations from non-parabolic dispersions. *Nat. Commun.* **12**, 6213 (2021).
10. Belopolski, I. et al. Observation of a linked-loop quantum state in a topological magnet. *Nature* **604**, 647–652 (2022).
11. Collins, J. L. et al. Electric-field-tuned topological phase transition in ultrathin Na_3Bi. *Nature* **564**, 390–394 (2018).
12. Osterhoudt, G. B. et al. Colossal mid-infrared bulk photovoltaic effect in a type-I Weyl semimetal. *Nat. Mater.* **18**, 471–475 (2019).
13. Tsai, H. et al. Electrical manipulation of a topological antiferromagnetic state. *Nature* **580**, 608–613 (2020).
14. Cheng, B. et al. Efficient terahertz harmonic generation with coherent acceleration of electrons in the Dirac semimetal Cd_3As_2. *Phys. Rev. Lett.* **124**, 117402 (2020).
15. Kovalev, S. et al. Non-perturbative terahertz high-harmonic generation in the three-dimensional Dirac semimetal Cd_3As_2. *Nat. Commun.* **11**, 2451 (2020).
16. Baireuther, P., Tworzydło, J., Breitkreiz, M., Adagideli, I. & Beenakker, C. W. J. Weyl-Majorana solenoid. *New J. Phys.* **19**, 025006 (2017).
17. Sakai, A. et al. Iron-based binary ferromagnets for transverse thermoelectric conversion. *Nature* **581**, 53–57 (2020).
18. Mizuguchi, M. & Nakatsuji, S. Energy-harvesting materials based on the anomalous Nernst effect. *Sci. Technol. Adv. Mater.* **20**, 262–275 (2019).
19. Rajamathi, C. R. et al. Weyl semimetals as hydrogen evolution catalysts. *Adv. Mater.* **29**, 1606202 (2017).
20. Kotov, V. N., Uchoa, B., Pereira, V. M., Guinea, F. & Neto, A. H. C. Electron-electron interactions in graphene: current status and perspectives. *Rev. Mod. Phys.* **84**, 1067–1125 (2012).
21. Elias, D. C. et al. Dirac cones reshaped by interaction effects in suspended graphene. *Nat. Phys.* **7**, 701–704 (2011).
22. Witczak-Krempa, W., Knap, M. & Abanin, D. Interacting Weyl semimetals: characterization via the topological Hamiltonian and its breakdown. *Phys. Rev. Lett.* **113**, 136402 (2014).
23. Carlström, J. & Bergholtz, E. J. Strongly interacting Weyl semimetals: stability of the semimetallic phase and emergence of almost free fermions. *Phys. Rev. B* **98**, 241102 (2018).
24. Isobe, H. & Nagaosa, N. Coulomb interaction effect in Weyl fermions with tilted energy dispersion in two dimensions. *Phys. Rev. Lett.* **116**, 116803 (2016).
25. Bulmash, D., Liu, C.-X. & Qi, X.-L. Prediction of a Weyl semimetal in $Hg_{1-x-y}Cd_xMn_yTe$. *Phys. Rev. B* **89**, 081106 (2014).
26. Xu, G., Weng, H., Wang, Z., Dai, X. & Fang, Z. Chern semimetal and the quantized anomalous Hall effect in $HgCr_2Se_4$. *Phys. Rev. Lett.* **107**, 186806 (2011).
27. Hasan, M. Z., Xu, S.-Y., Belopolski, I. & Huang, S.-M. Discovery of Weyl fermion semimetals and topological Fermi arc states. *Annu. Rev. Condens. Matter Phys.* **8**, 289–309 (2017).
28. Burkov, A. A. & Balents, L. Weyl semimetal in a topological insulator multilayer. *Phys. Rev. Lett.* **107**, 127205 (2011).
29. Belopolski, I. et al. A novel artificial condensed matter lattice and a new platform for one-dimensional topological phases. *Sci. Adv.* **3**, e1501692 (2017).
30. Murakami, S. Phase transition between the quantum spin Hall and insulator phases in 3D: emergence of a topological gapless phase. *New J. Phys.* **9**, 356 (2007).
31. Nagaosa, N., Morimoto, T. & Tokura, Y. Transport, magnetic and optical properties of Weyl materials. *Nat. Rev. Mater.* **5**, 621–636 (2020).
32. Wan, X., Turner, A. M., Vishwanath, A. & Savrasov, S. Y. Topological semimetal and Fermi-arc surface states in the electronic structure of pyrochlore iridates. *Phys. Rev. B* **83**, 205101 (2011).
33. Okazaki, Y. et al. Quantum anomalous Hall effect with a permanent magnet defines a quantum resistance standard. *Nat. Phys.* **18**, 25–29 (2022).
34. Zhang, H. et al. Topological insulators in Bi_2Se_3, Bi_2Te_3 and Sb_2Te_3 with a single Dirac cone on the surface. *Nat. Phys.* **5**, 438–442 (2009).
35. Liu, C.-X. et al. Model Hamiltonian for topological insulators. *Phys. Rev. B* **82**, 045122 (2010).
36. Burkov, A. A. Anomalous Hall effect in Weyl metals. *Phys. Rev. Lett.* **113**, 187202 (2014).
37. Mogi, M. et al. Experimental signature of the parity anomaly in a semi-magnetic topological insulator. *Nat. Phys.* **18**, 390–394 (2022).

38. Ong, N. P. & Liang, S. Experimental signatures of the chiral anomaly in Dirac–Weyl semimetals. *Nat. Rev. Phys.* **3**, 394–404 (2021).
39. Kandala, A., Richardella, A., Kempinger, S., Liu, C.-X. & Samarth, N. Giant anisotropic magnetoresistance in a quantum anomalous Hall insulator. *Nat. Commun.* **6**, 7434 (2015).
40. Liang, S. et al. Experimental tests of the chiral anomaly magnetoresistance in the Dirac-Weyl semimetals Na_3Bi and GdPtBi. *Phys. Rev. X* **8**, 031002 (2018).
41. Onoda, S., Sugimoto, N. & Nagaosa, N. Quantum transport theory of anomalous electric, thermoelectric, and thermal Hall effects in ferromagnets. *Phys. Rev. B* **77**, 165103 (2008).
42. Yang, S.-Y. et al. Giant, unconventional anomalous Hall effect in the metallic frustrated magnet candidate, KV_3Sb_5. *Sci. Adv.* **6**, eabb6003 (2020).
43. Liu, E. et al. Giant anomalous Hall effect in a ferromagnetic kagome-lattice semimetal. *Nat. Phys.* **14**, 1125–1131 (2018).

Methods

Equivalence to the Burkov–Balents theory

To give another perspective on $(Cr,Bi)_2Te_3$, we consider the well-known Burkov–Balents multilayer, which offers the simplest theoretical recipe for a magnetic Weyl semimetal, but remains unrealized so far[28]. This model consists of layers of a topological insulator similar to Bi_2Te_3, layers of a trivial insulator and ferromagnetism. The multilayer hosts a stack of coupled two-dimensional Dirac cones, which hybridize with one another to produce an emergent three-dimensional electronic structure hosting a single pair of Weyl points (Extended Data Fig. 1). The Hamiltonian is

$$H_{BB}=\sum_{i,j}[v_F(-\sigma_y k_x+\sigma_x k_y)\tau_z\delta_{ij}+J\sigma_z\delta_{ij}+t\tau_x\delta_{ij}-u\tau_+\delta_{i,j+1}-u\tau_-\delta_{i,j-1}]c_i^\dagger c_j \quad (2)$$

Here the first term captures the two-dimensional Dirac cone living at each interface within the stack, t represents the hopping amplitude across the topological insulator layer and u represents the hopping amplitude across the trivial insulator layer. J sets the ferromagnetic exchange splitting, so that $J>0$ corresponds to upward magnetization and $J<0$ corresponds to downward magnetization. There are two bands arising from the Dirac cone and two Dirac cones per unit cell, giving a four-band model. For convenience, we define t and u with opposite signs. Summation over k_x, k_y and the lattice basis is implied. In momentum space, we have

$$\begin{aligned}&H_{BB}=\sum_k c_k^\dagger h(\mathbf{k})c_k,\\&h(\mathbf{k})=v_F(-\sigma_y k_x+\sigma_x k_y)\tau_z+J\sigma_z+(te^{ik_z a}-ue^{-ik_z b})\tau_+ +\text{h.c.}\end{aligned} \quad (3)$$

in which a is the thickness of the topological layer and b is the thickness of the trivial layer. This is equivalent to equation (9) in ref. 28. Expanding around the Γ point, $k_z=0$, we obtain

$$h(\mathbf{k})_{BB}=v_F(-\sigma_y k_x+\sigma_x k_y)\tau_z+J\sigma_z+(t-u)\tau_x-k_z(ta+ub)\tau_y \quad (4)$$

This low-energy effective theory captures all of the electronic states near the Fermi level and can be viewed as governing the transport and low-frequency optical response of the system. Despite considerable interest, it has been challenging to realize the Burkov–Balents proposal directly[29,44,45]. At the same time, it is intriguing to note that $(Cr,Bi)_2Te_3$ is also based on Bi_2Te_3 and similarly shows a single pair of Weyl points. This suggests a close relationship to the Burkov–Balents model. Indeed, bulk Bi_2Te_3 itself can be viewed as a stack of coupled two-dimensional Dirac cones with $t<u$. In fact, $h(\mathbf{k})_{(Cr,Bi)_2Te_3}$ (equation (1)) and $h(\mathbf{k})_{BB}$ (equation (4)) are equivalent up to a unitary transformation and describe the same physics. Specifically, $h(\mathbf{k})_{(Cr,Bi)_2Te_3}$ and $h(\mathbf{k})_{BB}$ can be related by

$$h(\mathbf{k})_{BB}=U^\dagger h(\mathbf{k})_{(Cr,Bi)_2Te_3}U,\quad U=\frac{1}{\sqrt{2}}\begin{pmatrix}-1&-1&0&0\\-i&i&0&0\\0&0&1&1\\0&0&-i&i\end{pmatrix} \quad (5)$$

Under this transformation, $m\tau_z\leftrightarrow(t-u)\tau_x$ and $v_F k_z\sigma_z\tau_x\leftrightarrow -k_z(ta+ub)\tau_y$. Intuitively, if the topological insulator layers are very thin, the system should essentially become a ferromagnetic trivial insulator. In this regime, the hopping across the topological layer dominates, $t\gg u$, so $t-u>0$ and we see that the mass gap is trivial. By contrast, if the trivial insulator layers are very thin, the system is essentially a ferromagnetic topological insulator. This corresponds to $u\gg t$, so $t-u<0$ and the mass gap is topological. We have shown that the two models are equivalent and homogeneously doped $(Cr,Bi)_2Te_3$ can be viewed as realizing the experimentally challenging Burkov–Balents proposal.

Sample synthesis

$(Cr,Bi)_2Te_3$, $(Cr,Bi,Sb)_2Te_3$ and $(Cr,In,Bi,Sb)_2Te_3$ films were synthesized by molecular beam epitaxy (MBE) in a system equipped with standard Knudsen cells and maintained at a base pressure of 10^{-7} Pa. Films were deposited on epi-ready semi-insulating InP(111)A substrates that were chemically etched by 10% H_2SO_4, as well as BaF_2(111). Substrates were maintained during film synthesis at a growth temperature of 200 °C. The nominal composition of films was determined by beam equivalent pressures of Cr, In, Bi, Sb and Te fluxes, calibrated before film growth. The beam pressure of Te was set at a ratio of 40:1 relative to the cation elements, to suppress Te vacancies. X-ray diffraction patterns showed pronounced Laue fringes, no Cr_2Te_3 impurity peaks and sharp rocking curves, suggestive of high crystalline quality despite the comparatively high Cr doping level (Supplementary Figs. 3 and 4). The typical growth rate was 1 nm per 4 min, as determined by low-angle Laue fringes. To prevent deterioration in atmosphere, films were capped by 3 nm of AlO_x using atomic layer deposition at room temperature immediately after being removed from the MBE system. The actual Cr level was later calibrated through inductively coupled plasma mass spectroscopy (ICP-MS) and found to be higher than the nominal level fixed by beam equivalent pressure $x_{ICP\text{-}MS}\approx 5.7\times x_{nominal}$ (Extended Data Fig. 4). Hall bar devices of typical size 100 μm × 100 μm were fabricated using standard ultraviolet photolithography with Ar ion milling. Electrodes were deposited by electron beam evaporation of Ti (5 nm) followed by Au (45 nm).

Transport measurements

The electrical resistance was measured using a Quantum Design Physical Property Measurement System (PPMS) at temperatures of 2–300 K under magnetic fields up to 9 T and an excitation current of 10 μA. For compositions A and B, a bare film was measured, with Hall bars defined by gold wires fixed by Ag epoxy at distances of several millimetres. All other compositions were measured using lithographically patterned Hall bars with W and L of typical size 100 μm. The resistivity was extracted by scaling the resistance by the sample dimensions, $\rho_{xx}^{2D}=R_{xx}W/L$, $\rho_{yx}=R_{yx}$ and σ^{2D} was obtained by inverting the ρ^{2D} tensor. See Extended Data Fig. 3 for the resistivity measurements used to plot Fig. 1d,e. The three-dimensional bulk resistivity and conductivity were calculated using the film thickness h, $\rho=\rho^{2D}h$ and $\sigma=\sigma^{2D}/h$. The Weyl point separation was extracted from the three-dimensional conductivity as described in the main text, which gives Δk_{Weyl} in units of $Å^{-1}$. The size of the bulk Brillouin zone in k_z is $2\pi/c$, in which c is the lattice constant of $(Cr,Bi)_2Te_3$. The Weyl point separation was then obtained as a percentage of $2\pi/c$, so that 100% corresponds to the Weyl points meeting up at the boundary of the bulk Brillouin zone. Equivalently, the Weyl point separation is defined so that 100% corresponds to the phase transition into a three-dimensional QAH state, in which all k_x–k_y slices of the bulk Brillouin zone host a Chern number $C=1$ (Supplementary Fig. 6).

Density functional theory

Calculations were performed within the density functional theory (DFT)[46] framework with the projector augmented wave basis, using the Vienna Ab initio Simulation Package[47]. The Perdew–Burke–Ernzerhof-type generalized gradient approximation[48] was used to describe the exchange-correlation energy. A plane-wave cut-off of 300 eV was used and a 12 × 12 × 6 k-mesh was chosen to sample the bulk Brillouin zone. The total energies were converged to 10^{-6} eV. SOC was taken into account self-consistently to treat relativistic effects. See Extended Data Table 1 for crystal structures.

For calculations under disorder, we start from a supercell of Sb_2Te_3 that is four quintuple layers thick. We consider eight different doping configurations for $(Cr_{0.125}Sb_{0.875})_2Te_3$, in which the Cr atoms are placed

at different lattice sites (Supplementary Fig. 5). All doping configurations individually preserve inversion symmetry. The lattice constants and atomic positions of each configuration are fully relaxed, with total force converging to −0.01 eV Å^{-1}. For electronic structure calculations, a plane-wave cut-off of 300 eV was used and a 3 × 6 × 3 k-mesh was chosen to sample the bulk Brillouin zone. The total energies were converged to 10^{-6} eV. The resulting on-site potentials were averaged out. See the Supplementary Information for the structures of the eight dopant configurations.

Numerical calculations under disorder

We describe an approach to numerically compute Chern numbers in topological phases, both with and without magnetic disorder, focusing particularly on Weyl semimetals. From the low-energy effective theory equation (1), we specialize to a lattice model[49]

$$\begin{aligned} h(\mathbf{k})_{\text{lattice}} = {} & v_{\text{F}}[\sin(k_x a)\sigma_x + \sin(k_y a)\sigma_y + \sin(k_z a)\sigma_z]\tau_x \\ & + A_0[m + 3 - \cos(k_x a) - \cos(k_y a) - \cos(k_z a)]\tau_z + J\sigma_z \end{aligned} \tag{6}$$

To fit the energy spectrum from the DFT calculations (Fig. 1c), we use the values of the parameters $v_{\text{F}} = 40$ meV and $A_0 = -32.1$ meV. In the absence of magnetization ($J = 0$), increasing the mass gap m leads to a phase transition at $m = 0$ from a topological insulator to a trivial insulator.

We simplify the problem by considering a cubic lattice of thickness $L_z = 30$ unit cells. To distinguish different topological phases, we first calculate the Chern number in momentum space $k = (k_x, k_y)$ (ref. 50)

$$C = \frac{1}{2\pi}\int_{\text{BZ}} \text{tr}\{\hat{P}(k)[\partial_{k_x}\hat{P}(k), \partial_{k_y}\hat{P}(k)]\}d^2k, \tag{7}$$

in which $P(k)$ represents the projector matrix onto the occupied states of the lattice Hamiltonian. When magnetization is introduced and mass m varies, the pristine phases split into a Chern insulator, a Weyl semimetal, and a trivial insulator. These phases are indicated by different values of the Chern number, as shown in Fig. 3.

We now introduce disordered magnetization $J = J_0 + J'(r)$, in which J_0 indicates the average magnetization. To reduce computational load, we consider magnetic disorder $J'(r)\sigma_z\tau_0$ that exhibits random normal distributions only in the x and z directions while remaining homogeneous in the y direction. With this magnetic disorder, the lattice Hamiltonian in x–z real space can be rewritten in the second quantization form

$$\begin{aligned} \hat{H}_{\text{lattice}}(k_y) = \sum_r \Big\{ & C_r^\dagger[A_0(m + 3 - \cos k_y a)\sigma_0\tau_z \\ & + v_{\text{F}}\sin k_y a\sigma_y\tau_x + (J_0 + \delta J_r)\sigma_z\tau_0]C_r \\ & + \frac{1}{2}[C_{r+a\hat{x}}^\dagger(\text{i}v_{\text{F}}\sigma_x\tau_x - A_0\sigma_0\tau_z)C_r \\ & + C_{r+a\hat{z}}^\dagger(\text{i}v_{\text{F}}\sigma_z\tau_x - A_0\sigma_0\tau_z)C_r + \text{h.c.}]\Big\} \end{aligned} \tag{8}$$

Numerically, we consider periodic boundaries in the x and y directions and an open boundary in the z direction. Owing to the large size of the Hamiltonian matrix, the system size is chosen to be $L_x \times L_y \times L_z = 34 \times 36 \times 30$. To obtain the Chern number, we diagonalize the Hamiltonian $\hat{H}_{\text{lattice}}(k_y)$ to obtain the projector matrix $P(k_y)$ for the occupied states. The Chern number equation (7) in the presence of disorder in the x direction can be rewritten[51] as

$$C = \int_{\text{BZ}_y} \text{tr}\left\{\hat{X}_{\text{e}}^{-1}P(k_y)\left[\hat{X}_{\text{e}}P(k_y), \frac{\partial}{\partial k_y}P(k_y)\right]\right\}dk_y/2\pi\text{i}, \tag{9}$$

in which the operator $\hat{X}_{\text{e}} = \text{e}^{2\pi\text{i}\hat{X}/L_x}$ for the real space. We take the standard deviation of the strength of the disorder to be approximately $\sigma(J) = 10$ meV, based on experiments[52]. For each fixed J_0 and m, we run ten different disorder realizations with the same $\sigma(J)$ and average the results.

Data availability

All data relevant to the conclusions of this study are available from Zenodo[53].

44. Zhao, Y.-F. et al. Tuning the Chern number in quantum anomalous Hall insulators. *Nature* **588**, 419–423 (2020).
45. Lei, C., Chen, S. & MacDonald, A. H. Magnetized topological insulator multilayers. *Proc. Natl Acad. Sci.* **117**, 27224–27230 (2020).
46. Hohenberg, P. & Kohn, W. Inhomogeneous electron gas. *Phys. Rev.* **136**, B864 (1964).
47. Kresse, G. & Fürthmueller, J. Efficient iterative schemes for *ab initio* total-energy calculations using a plane-wave basis set. *Phys. Rev. B* **54**, 11169 (1996).
48. Perdew, J. P., Burke, K. & Ernzerhof, M. Generalized gradient approximation made simple. *Phys. Rev. Lett.* **77**, 3865 (1996).
49. Qi, X.-L., Hughes, T. L. & Zhang, S.-C. Topological field theory of time-reversal invariant insulators. *Phys. Rev. B* **78**, 195424 (2008).
50. Thouless, D. J., Kohmoto, M., Nightingale, M. P. & den Nijs, M. Quantized Hall conductance in a two-dimensional periodic potential. *Phys. Rev. Lett.* **49**, 405 (1982).
51. Prodan, E., Hughes, T. L. & Bernevig, B. A. Entanglement spectrum of a disordered topological Chern insulator. *Phys. Rev. Lett.* **105**, 115501 (2010).
52. Lee, I. et al. Imaging Dirac-mass disorder from magnetic dopant atoms in the ferromagnetic topological insulator $Cr_x(Bi_{0.1}Sb_{0.9})_{2-x}Te_3$. *Proc. Natl Acad. Sci.* **112**, 1316–1321 (2015).
53. Belopolski, I. et al. Source data for 'Synthesis of a semimetallic Weyl ferromagnet with point Fermi surface'. *Zenodo* https://doi.org/10.5281/zenodo.13969155 (2025).
54. Nagaosa, N., Sinova, J., Onoda, S., MacDonald, A. H. & Ong, N. P. Anomalous Hall effect. *Rev. Mod. Phys.* **82**, 1539–1592 (2010).

Acknowledgements I.B. acknowledges discussions on transport measurements with M. T. Birch and discussions about BaF_2 substrates with M. Nakamura. I.B. acknowledges M. Hirschmann for insights on the theory. I.B. and R.Y. acknowledge film synthesis by T. Ueda. We acknowledge K. Manna for transport data on Co_2MnGa, C. Zhang for transport data on TaAs and Y. Wang, S.-Y. Yang and M. Ali for anomalous Hall scaling data on reference materials. I.B. acknowledges discussions on Weyl physics with L. Tai, M. Mogi, H. Isobe, T. A. Cochran, D. S. Sanchez, Q. Ma, S.-Y. Xu, J. Checkelsky and K. Yasuda. We are grateful to all members of the RIKEN Center for Emergent Matter Science (CEMS) for discussions. This work was supported by the Japan Society for the Promotion of Science (JSPS), KAKENHI grant 23H05431 (Y. Tokura), 24K17020 (Y.S.), 24H01607 (M.H.), 22H04958 (M. Kawasaki), 24H00197 (N.N.), 24H02231 (N.N.) and 23H01861 (M. Kawamura); and by the Japan Science and Technology Agency (JST) FOREST JPMJFR2238 (M.H.). N.N. was also supported by the RIKEN TRIP Initiative. C.-K.C. was supported by JST Presto grant JPMJPR2357 and partially supported by JST as part of Adopting Sustainable Partnerships for Innovative Research Ecosystem (ASPIRE) grant JPMJAP2318. This work was further supported by the RIKEN TRIP Initiative (Many-Body Electron Systems). Work at Nanyang Technological University was supported by the National Research Foundation, Singapore, under its Fellowship Award (NRF-NRFF13-2021-0010); the Agency for Science, Technology and Research (A*STAR) under its Manufacturing, Trade and Connectivity (MTC) Individual Research Grant (IRG) (grant M23M6c0100); a Singapore Ministry of Education (MOE) Academic Research Fund Tier 3 grant (MOE-MOET32023-0003); a Singapore Ministry of Education (MOE) AcRF Tier 2 grant (MOE-T2EP50222-0014); and the Nanyang Assistant Professorship grant (NTU-SUG).

Author contributions Y.To. and N.N. supervised the project. I.B. conceived the research. R.W. and I.B. synthesized thin films and fabricated devices with help from Y.S. and S.N. and under the guidance of R.Y., M.Kawam., A.T., K.S.T., M.Kawas. and Y.To. Y.Z., S.S. and Y.J. performed first-principles calculations under the supervision of G.C. Y.K., Y.O., I.B. and X.-X.Z. acquired and analysed Terahertz spectra under the guidance of Y.Ta., N.N. and Y.To. R.W. and I.B. performed transport measurements with help from Y.S., Y.F. and M.H. C.-K.C. performed the numerical calculations with I.B. and Y.S. I.B. wrote the theory under the guidance of C.-K.C., N.N. and Y.To. I.B. wrote the manuscript, with contributions from all authors.

Competing interests The authors declare no competing interests.

Additional information

Supplementary information The online version contains supplementary material available at https://doi.org/10.1038/s41586-024-08330-y.

Correspondence and requests for materials should be addressed to Ilya Belopolski or Yoshinori Tokura.

Peer review information *Nature* thanks Aris Alexandradinata and the other, anonymous, reviewer(s) for their contribution to the peer review of this work. Peer reviewer reports are available.

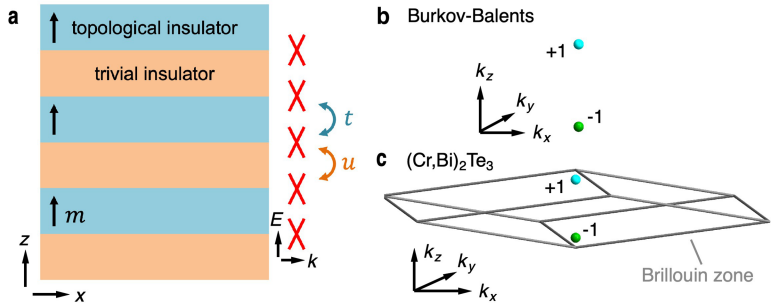

Extended Data Fig. 1 | Burkov–Balents proposal without a multilayer. a, The original theoretical model considers a stack of alternating layers of topological and trivial insulators hosting two-dimensional Dirac cones (red cones) at each interface. These interface states hybridize with one another with amplitude t across the topological layer and u across the trivial layer; there is also ferromagnetism m (ref. 28). **b**, The resulting electronic structure shows a semimetallic Weyl phase with two Weyl points along k_z (cyan and green dots). **c**, We circumvent the complicated multilayer structure and realize the same electronic structure as the Burkov–Balents proposal in homogeneously doped thin films of $(Cr,Bi)_2Te_3$.

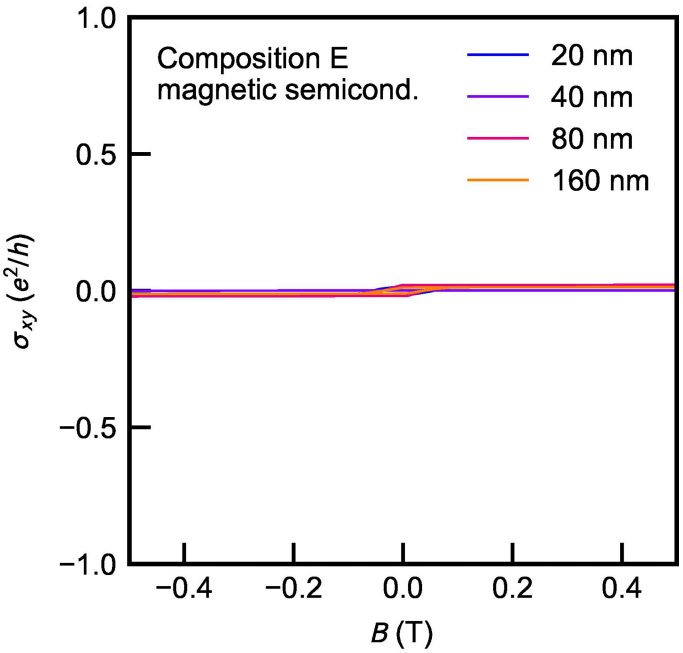

Extended Data Fig. 2 | Systematics on the magnetic semiconductor. AHE of composition E, a trivial magnetic semiconductor. The film shows negligible AHE $\ll 1\,e^2/h$ for all thicknesses.

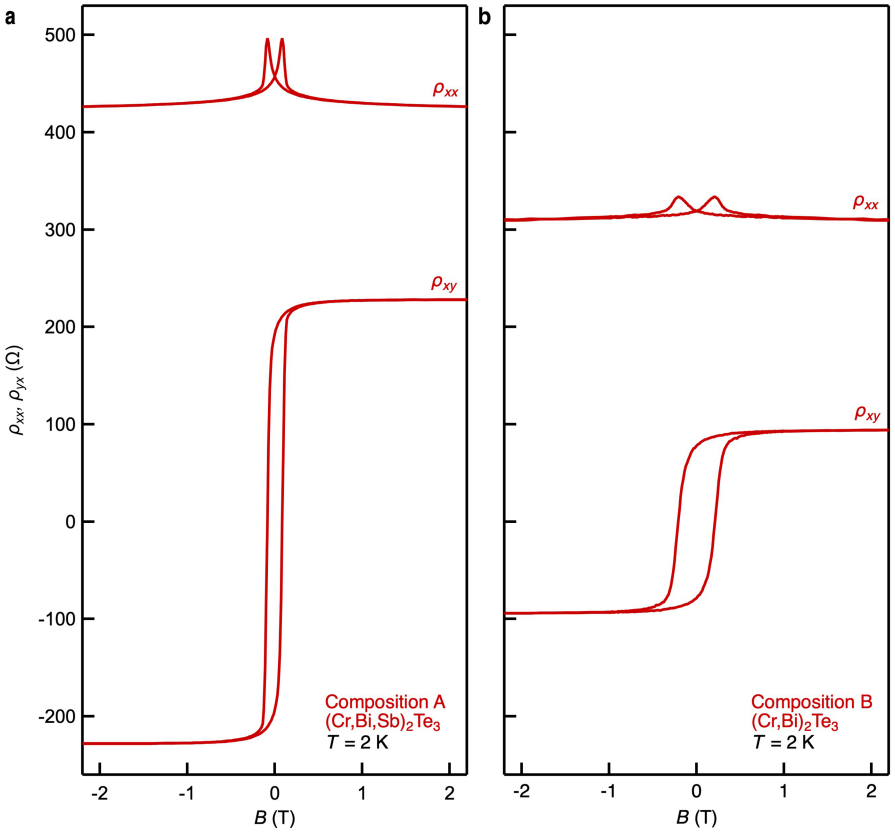

Extended Data Fig. 3 | Resistivity of compositions A and B. Measured $\rho_{xx}(B)$ and $\rho_{yx}(B)$ for $(Cr,Bi,Sb)_2Te_3$ and $(Cr,Bi)_2Te_3$, used to calculate the conductivity $\sigma(B)$ in Fig. 1d,e.

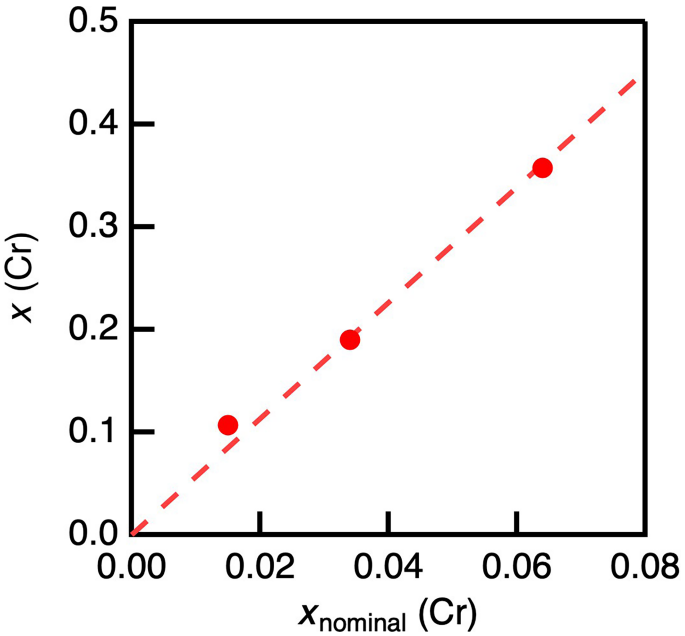

Extended Data Fig. 4 | Measured Cr composition. Chromium content x for a series of $(Cr,Bi,Sb)_2Te_3$ films measured by ICP-MS, plotted against the nominal chromium content $x_{nominal}$ determined by beam flux pressure during film synthesis. We observe $x \approx 5.7 \times x_{nominal}$.

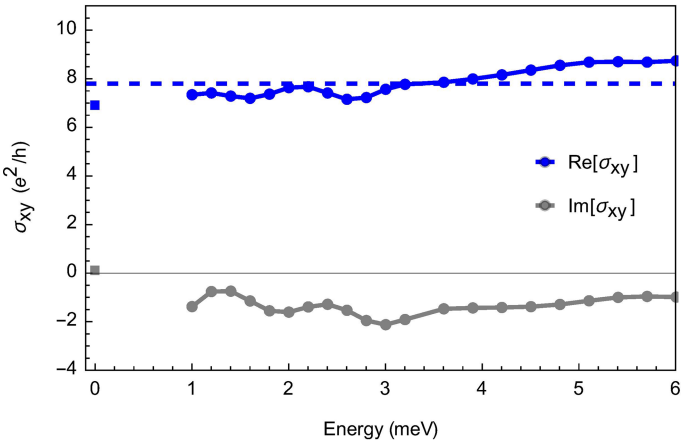

Extended Data Fig. 5 | Optical conductivity. Frequency-dependent Hall conductivity in the terahertz range for a Weyl film, composition C of thickness $h = 160$ nm. The low-frequency $\Re[\sigma_{xy}]$ is approximately constant and consistent with dc transport (square points).

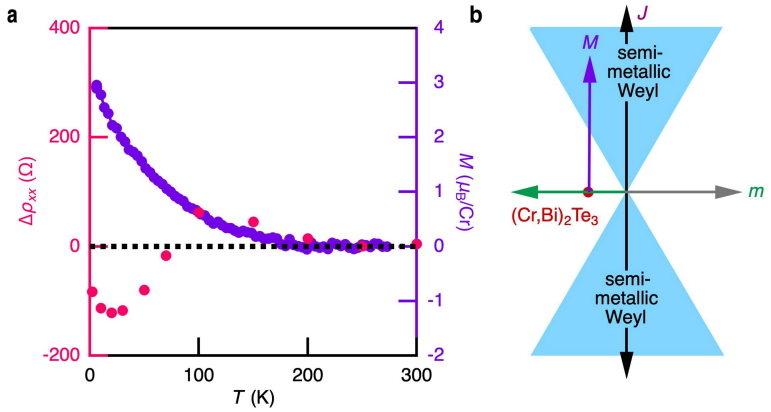

Extended Data Fig. 6 | Temperature dependence and angular magnetoresistance. a, Temperature dependence of the angular magnetoresistance at $x_{Cr} = 0.13$ and $x_{In} = 0$ (included in Fig. 3b, between compositions C and D). **b**, The change in sign of the angular magnetoresistance suggests that, as the magnetization *M* develops on cooling, the system shows a transition from a Chern insulator to a semimetallic Weyl phase.

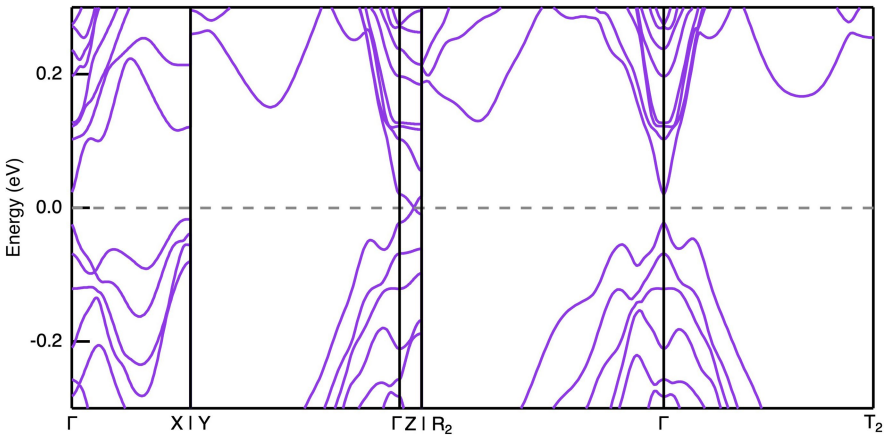

Extended Data Fig. 7 | Wide-range electronic structure of $Cr_{0.25}Sb_{1.75}Te_3$ under Cr disorder. The electronic structure was calculated for an Sb_2Te_3 supercell with one of eight Sb atoms replaced by Cr dopant atoms, under several dopant disorder configurations. The resulting on-site potentials were averaged out. The disordered electronic structure reveals a single pair of Weyl points along Γ–Z, with Weyl point separation $\Delta k_z = 48\%$, and no other bands at the Fermi level.

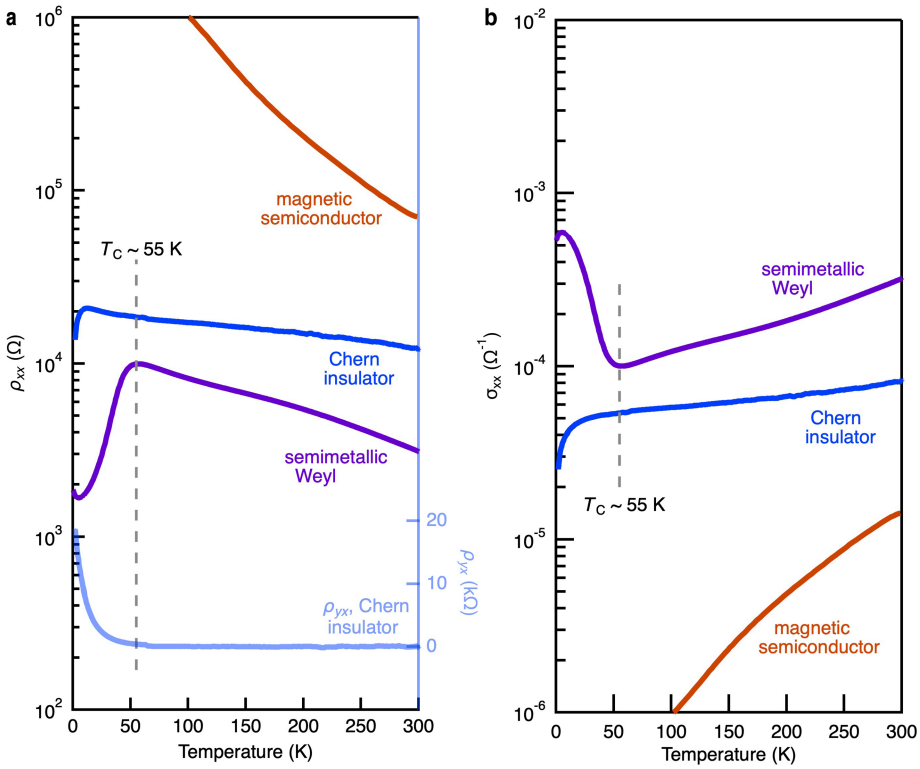

Extended Data Fig. 8 | Distinguishing topological phases through $\rho_{xx}(T)$ and $\sigma_{xx}(T)$. a, Temperature dependence of the resistivity for a Chern insulating composition, similar to composition D (blue); semimetallic Weyl composition C (purple); and magnetic semiconductor at higher indium doping, $z = 0.12$ (orange). The Curie temperature for the Chern insulating composition is $T_C \approx 55$ K, obtained from the onset of the Hall resistivity (light blue). Composition C shows a similar T_C. Notably, the Weyl composition C shows a marked metallic downturn in $\rho_{xx}(T)$ below T_C, whereas the Chern insulator film shows no notable feature around T_C. The metallic downturn provides an extra signature of the emergence of a semimetallic Weyl state. **b**, $\sigma_{xx}(T)$ for the same films, obtained from the resistivity.

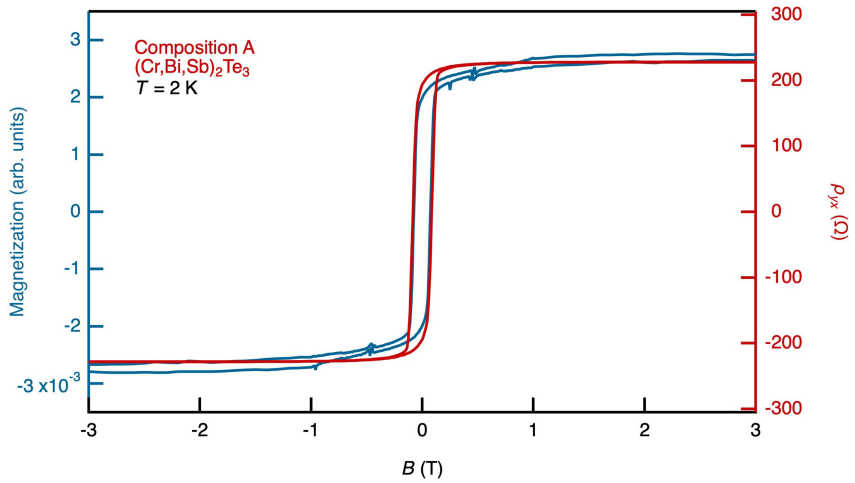

Extended Data Fig. 9 | AHE. Magnetization $M(B)$ and Hall resistivity $\rho_{yx}(B)$ for composition A. We see that $\rho_{yx}(B)$ is approximately proportional to $M(B)$, suggesting that the observed Hall resistivity mainly consists of an AHE[54].

Extended Data Table 1 | Crystal structures used for ab initio calculations

Crystal	Lattice (Å, deg.)	Atomic coordinates (fractional)			
		Atom	*x*	*y*	*z*
$Cr_2Sb_4Te_9$	$a = 4.3039$	Cr1	0.00000	0.00000	0.39580
$P\bar{3}m1$	$b = 4.3039$	Cr2	0.00000	0.00000	0.60420
	$c = 31.7773$	Sb1	0.66667	0.33333	0.72913
	$\alpha = \beta = 90°$	Sb2	0.66667	0.33333	0.72913
	$\gamma = 120°$	Sb3	0.33333	0.66667	0.27087
		Sb4	0.33333	0.66667	0.06246
		Te1	0.00000	0.00000	0.21745
		Te2	0.00000	0.00000	0.78255
		Te3	0.66667	0.33333	0.55079
		Te4	0.33333	0.66667	0.44921
		Te5	0.66667	0.33333	0.33333
		Te6	0.33333	0.66667	0.66667
		Te7	0.33333	0.66667	0.88412
		Te8	0.66667	0.33333	0.11588
		Te9	0.00000	0.00000	0.00000
$Cr_2Bi_4Te_9$	$a = 4.43676$	Cr1	0.00000	0.00000	0.60124
$P\bar{3}m1$	$b = 4.43676$	Cr2	0.00000	0.00000	0.39876
	$c = 31.31840$	Bi1	0.33333	0.66667	0.26791
	$\alpha = \beta = 90°$	Bi2	0.33333	0.66667	0.06542
	$\gamma = 120°$	Bi3	0.66667	0.33333	0.93458
		Bi4	0.66667	0.33333	0.73209
		Te1	0.00000	0.00000	0.00000
		Te2	0.00000	0.00000	0.21308
		Te3	0.66667	0.33333	0.12026
		Te4	0.66667	0.33333	0.33333
		Te5	0.66667	0.33333	0.54641
		Te6	0.33333	0.66667	0.45359
		Te7	0.33333	0.66667	0.66667
		Te8	0.33333	0.66667	0.87974
		Te9	0.00000	0.00000	0.78692

Lattice unit cells and atomic coordinates of $(Cr,Sb)_2Te_3$ and $(Cr,Bi)_2Te_3$.